Observations of an extreme atmospheric river storm with a diverse sensor network

B. J. Hatchett*[1], Q. Cao[2], P.B. Dawson[3], C. J. Ellis[4], C. W. Hecht[4], B. Kawzenuk[4], J. T. Lancaster[5], T. Osborne[4], A. M. Wilson[4], M. L. Anderson[6], M. D. Dettinger[4], J. Kalansky[4], M. L. Kaplan[7], D. P. Lettenmaier[2], N. S. Oakley[1,4], F. M. Ralph[4], D.W. Reynolds[8], A. B. White[9], M. Sierks[4], E. Sumargo[4]

[1]Western Regional Climate Center, Reno, Nevada, USA

[2]Department of Geography, University of California, Los Angeles, CA, USA

[3]California Volcano Observatory, U.S. Geological Survey, Moffett Field, California, USA

[4]Center for Western Weather and Water Extremes, Scripps Institution of Oceanography, University of California, San Diego, La Jolla, California, USA

[5]California Geological Survey, Sacramento, California, USA

[6]California Department of Water Resources, Sacramento, California, USA

[7]Applied Meteorology Program, Embry-Riddle Aeronautical University, Prescott, Arizona, USA

[8]Department of Atmospheric and Oceanic Sciences, Colorado University, Boulder, Colorado, USA

[9]NOAA/Earth System Research Laboratory/Physical Sciences Division, Boulder, Colorado, USA

*Corresponding author: Benjamin Hatchett (benjamin.hatchett@gmail.com)

Key Points:

- A multi-tiered observational network in California is evaluated during an extreme atmospheric river storm spanning 13-15 February 2019
- The network validates record precipitable water and detects mesoscale atmospheric processes driving flood, snowfall, and mass wasting events
- Diverse, high frequency observational networks are valuable investments to aid water resource management and natural hazard mitigation

Abstract

Observational networks enhance real-time situational awareness for emergency and water resource management during extreme weather events. We present examples of how a diverse, multi-tiered observational network in California provided insights into hydrometeorological processes and impacts during a three-day atmospheric river storm centered on 14 February 2019. This network, which has been developed over the past two decades, aims to improve understanding and mitigation of effects from extreme storms influencing water resources and natural hazards. We combine atmospheric reanalysis output and additional observations to show how the network allows for: 1) the validation of record cool season precipitable water observations over southern California, 2) the identification of phenomena that produce natural hazards and present difficulties for short-term weather forecast models, such as extreme precipitation amounts and snow level variability, 3) the use of soil moisture data to improve hydrologic model forecast skill in northern California's Russian River basin, and 4) the combination of meteorological data with seismic observations to "observe" a large avalanche on Mount Shasta. This case study highlights the value of investments in diverse observational assets and the importance of continued support and synthesis of diverse observations to characterize climatological context and advance understanding of processes modulating extreme weather.

1 Introduction

California's complex terrain, biogeographical diversity, proximity to the data-sparse North Pacific Ocean, and large population and economy provide an environment both dependent upon and highly susceptible to weather and climate extremes (Lundquist & Cayan, 2007; Cayan et al., 2016). These include extreme precipitation events, flooding, land-surface mass wasting, multi-year droughts and pluvials, heat waves, and wildfires (Ralph et al., 2006; Dettinger et al., 2011; Swain, 2015; Lamjiri et al., 2017; Oakley et al., 2018a,b). Water resources in California rely on precipitation and snowpack resulting in large part from landfalling atmospheric rivers (ARs) associated with cool season midlatitude cyclones (Dettinger et al., 2011; Rutz et al., 2014). However, the extreme precipitation and hydrometeorological impacts associated with many of these storms bring significant emergency management challenges and expenses (Corringham et al., 2019; Ralph et al., 2019). Managing and reducing these challenges and costs requires accurate understanding of what, where, and when the various impacts are taking place. However, weather models initialized over data-poor locations such as oceans (e.g., Nardi et al., 2018) provide inadequate information. Other data sources are often limiting as well. This creates a need for networks of readily-available, high resolution, and diverse observations. Such networks facilitate tracking, evaluation, and anticipation of storm-related impacts and impact-triggering thresholds necessary for early warning of natural hazards and achievement of water resource management objectives (White et al., 2013; Ralph et al., 2014; Moore et al., 2015; Oakley et al., 2017, 2018b; Sterle et al., 2019; Uccellini & Ten Hoeve, 2019).

To accommodate these data needs in California, a multi-tiered network of observations (Table 1) has been implemented and expanded since the early 2000s (White et al., 2013; Ray & White, 2019). This network evolved from the goal of understanding extreme events in California to a broader vision aimed at observing the mountainous western United States (Ralph et al., 2014). The network includes sensors within a particular range of technology levels, novelty, and costs (Table 1) and is supported by a wide variety of agencies at the federal, state, county, and local

levels as well as private groups. Some components of the network, such as snow level radars and AR observatories (AROs), have been installed as part of the jointly-supported National Oceanic and Atmospheric Administration (NOAA)/California Department of Water Resources Hydrometeorology Testbed (HMT) and are tracked by the NOAA Observing System Council (White et al., 2013). Others, like the Global Navigation Satellite Systems/Global Positioning System (GNSS/GPS) network, leverage sensors with differing primary goals to extend precipitable water observations over land (e.g., Bevis et al., 1992). Lower tiers of the network include proven, cost-effective technology augmenting existing standard weather stations. These measurements are of common variables, such as soil moisture, snow water equivalent, and snow depth. Higher monitoring tiers, such as snow level radar, targeted dropsondes from offshore aircraft-based reconnaissance flights, and gap-filling radar, are more novel and costlier (White et al., 2013; Cordeira et al., 2017; Johnston et al., 2017; Cifelli et al., 2018).

We demonstrate how select data from this network, in conjunction with additional available atmospheric and hydrologic modeling and observational data, provides *a posteriori* insight into processes and impacts resulting from an extreme winter AR event, the "Valentine's Day Storm" spanning 13-15 February 2019. Three-day accumulated precipitation ranged from 100 to more than 200 mm (Figure 1a) and markedly increased soil moisture (Figure 1b-c). Impacts from this storm included riverine and alluvial fan flash flooding, evacuations from burned areas, avalanches, landslides, and disruptions to transportation and commerce from road closures. We focus on three regions of California (Figure 1a): southern California (region I), the southern Cascades and northern Sierra Nevada (region II), and the Russian River watershed (region III). We begin with a synoptic meteorological analysis (Section 3). Observations and impacts from each region are presented as separate sub-case studies (Sections 4-6) intending to highlight the added value the network provides with respect to understanding storm processes and impacts. We end with discussion regarding how such networks support the achievement of broader water resource management and natural hazard mitigation goals (Sections 7-8).

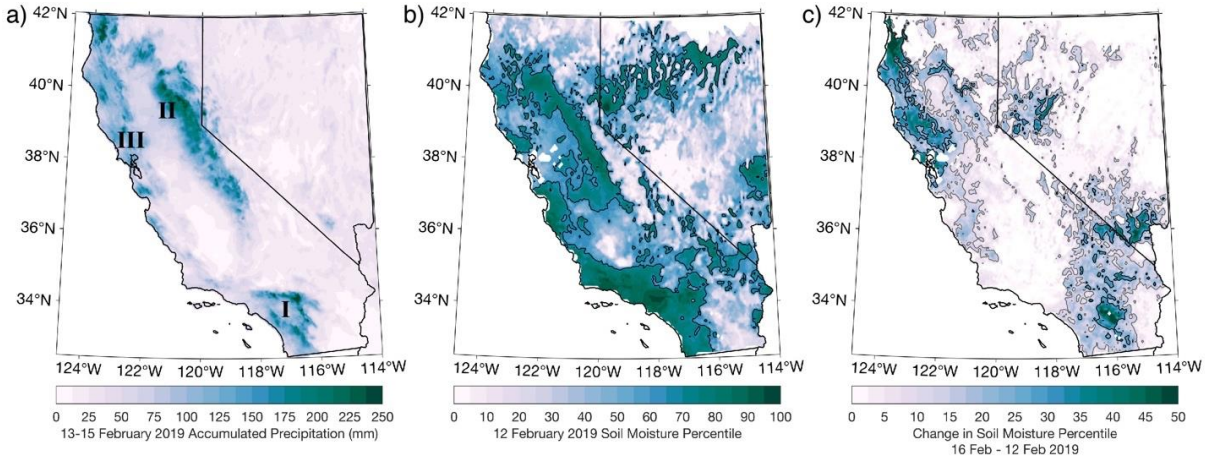

Figure 1: Event precipitation and soil moisture conditions prior to and following the storm. (a) Accumulated 13-15 February 2019 precipitation from the 4 km gridMET product (Abatzoglou, 2013) with focus regions of study: Region I (southern California), Region II (southern Cascades and northern Sierra Nevada), and Region III (Russian River watershed). (b) Antecedent soil

moisture percentiles on 12 February 2019 estimated from the Variable Infiltration Capacity model (Liang et al., 1994). Black contours enclose percentiles within the top tercile (66%) (c) Change in soil moisture percentile between 12 February and 16 February 2019. The grey and black contours enclose changes exceeding 10% and 25%, respectively.

2 Observational data and model products used

Our primary focus is on ground-based sensors with real-time data availability (Ralph et al., 2014), however we also utilize observations from aircraft, radiosondes and satellites as well as seismic observations. In addition, we leverage operational and reanalysis-based atmospheric model output to support interpretations of observational data. Information about the observational networks are provided in Table 1. We incorporate 0.5° x 0.625° horizontal resolution, three-hourly output from the Modern-Era Retrospective Reanalysis Version 2 (MERRA-2; Gelaro et al., 2017) to estimate return intervals of integrated vapor transport (IVT) and integrated water vapor (IWV). These return intervals are calculated over meteorological winters (December-February) spanning 1980-2019. We use potential vorticity on the 330 K surface from the hourly 0.5° Global Forecast System final analysis (GFS; NOAA Environmental Modeling Center, 2003) to diagnose Rossby wave breaking, a common precursor to extreme midlatitude weather events (e.g., Hu et al., 2017; Rondanelli et al., 2019), via the overturning of potential vorticity surfaces (Abatzoglou & Magnusdottir, 2006). Daily soil moisture percentiles corresponding to the soil root zone depth (1.4-2.53 m) are estimated using the Variable Infiltration Capacity model (VIC; Liang et al., 1994). Additional observations included: radiosondes launched from La Jolla, CA, two ALERT tipping bucket precipitation gauges in the Transverse and Peninsular Ranges, used by local government agencies for real-time flood management and early warnings, and data from four United States Geological Survey (USGS) Northern California Seismic Network seismometers installed on Mount Shasta (NCEDC, 2014). The seismic instruments are used to constrain the timing of a large avalanche event on Mount Shasta (southern Cascades) during the storm.

Table 1: Observational data and model output used.

Network	Details	Additional Information
Hydrometeorology Testbed (HMT) West Legacy Observing Network	A California Department of Water Resources network installed and operated by NOAA's Oceanic and Atmospheric Research (OAR) Physical Sciences Division (PSD). Instruments include: precipitation gauges and disdrometers, various wind and temperature profiling radars, GPS, stream level loggers, soil moisture probes, snow pillows, and more.	https://hmt.noaa.gov/
Snow Level Radars	NOAA Earth Systems Research Laboratory and California Department of Water Resources joint radar network allowing for novel measurements of bright band heights.	Johnston et al. (2017)
Atmospheric River Observatories (AROs)	Evolved from HMT-West, a small network with a combination of three to four instruments including radar wind profilers, GPS IWV sensors, standard surface meteorology stations, and in some cases snow level radar.	White et al. (2009)
GNSS/GPS	A global network originally developed for	https://www.suominet.ucar.edu/

	positioning, navigation, and time transfer that now has many more uses including atmospheric/climate studies due to their ability to measure zenith tropospheric delay as a function of temperature, pressure, and water vapor.	index.html https://hmt.noaa.gov/
Atmospheric River Reconnaissance	Observations by aircraft dropsondes (flight paths shown in Figure 3) and buoys in the Northeast Pacific Ocean intended to improve existing forecasts of ARs while supporting research to improve weather models, data assimilation methods, and reconnaissance targeting methods.	http://cw3e.ucsd.edu/arrecon_overview/
Radiosondes	Radiosonde observations are made throughout the country by NWS and compiled and made available by the University of Wyoming. Several other research groups, such as CW3E at Scripps, also record sounding data.	http://weather.uwyo.edu/upperair/sounding.html
Automated Local Evaluation in Real-Time (ALERT)	Wireless sensor network providing real-time flood warnings, but can also monitor wind, temperature, humidity barometric pressure, soil moisture, fuel moisture, and more.	https://www.alertsystems.org/index.php/about-us
USGS Water Data	Nationwide network of USGS sites with real-time or recent and historic stream gage data.	https://waterdata.usgs.gov/nwis/sw
Palomar Observatory National Weather Service Cooperative Observer (COOP) Network	Long-term, daily observations of temperature, precipitation, snowfall, and occasionally evaporation or soil temperature. Forms the United States component of the Global Historical Climatology Network-Daily.	https://www.ncdc.noaa.gov/data-access/land-based-station-data/land-based-datasets/cooperative-observer-network-coop
MIMIC-TPW2 IWV observations	An experimental global product of satellite-derived total precipitable water using morphological compositing of microwave integrated retrieval system (Liu & Weng, 2005) retrievals from operational microwave frequency observations. Supplementary Figure 1.	http://tropic.ssec.wisc.edu/real-time/mtpw2/ Wimmers & Velden (2010)
gridMET	A daily gridded dataset of high-spatial resolution (6 km) surface meteorological variables covering the contiguous US.	http://www.climatologylab.org/gridmet.html Abatzoglou (2013)
USGS Northern California Seismic Hazards program	USGS program, including comprehensive monitoring of earthquakes, that is part of the National Earthquake Hazards Reduction Program (NEHRP).	https://www.usgs.gov/natural-hazards/earthquake-hazards https://ncedc.org/
Sub-daily meteorological observations	Sub-daily observations supported by various agencies and available from the California Data Exchange Center (CDEC) and MesoWest.	mesowest.utah.edu/ http://cdec.water.ca.gov/

3 Large-scale atmospheric conditions

At 0600Z 13 February 2019 large-scale atmospheric conditions were characterized by amplified planetary waves and active cyclonic and anticyclonic Rossby wave breaking (RWB; Thorncroft et al., 1993; Abatzoglou & Magnusdottir, 2006) over the western and eastern margins of the North Pacific Basin, respectively (Figure 2a). The cyclonic RWB in the western Pacific induces cyclogenesis and promotes the formation of a downstream ridge near the dateline (180°W) and a persistent trough over the eastern Pacific (Moore et al., 2019). AR conditions (IVT exceeding 250 kg m^{-1} s^{-1}; Ralph et al., 2019) with strong poleward and eastward transport of moisture were

observed along the eastern flanks of the high potential vorticity air (Figure 2a), consistent with RWB and diabatic forcing of cyclogenesis (Hu et al., 2017).

Equatorward of the planetary-scale anticyclonic RWB, a zonally-extended coupled polar and subtropical trans-Pacific jet stream exceeding 40 m s^{-1} existed with the divergent left jet exit region positioned over northern-central California. A surface cyclone was located offshore of the northern California coast under the cyclonic shear side of the jet stream. The zonally-extended mid-upper tropospheric flow undercutting an amplified ridge with axis near the dateline is a favorable scenario for heavy precipitation in California (Underwood et al., 2009) with high snow levels (Hatchett et al., 2017a). The upper level jet, anticyclonic RWB in the polar stream, and subtropical moisture connection promoted elevated atmospheric moisture and moisture transport over southern California (Payne & Magnusdottir, 2014; Figure 2b-c). The southwesterly orientation of moisture transport established by cyclonic RWB in the subtropical jet stream (Figure 2a; Hu et al., 2017) enhanced upslope water vapor flux and helped produce heavy orographic precipitation (Ralph et al., 2013). Two plumes of water vapor transport are evident in the IVT field (Figure 3a). Both displayed modeled IVT values exceeding 1000 kg m^{-1} s^{-1} but very different IWV values (Figure 3b). The northern plume 1 is wind-dominated due to its lower values of IWV compared to the southern plume 2. These two branches appear to be the result of a merged RWB process where smaller-scale barotropic cyclonic wave breaking occurring in the subtropical jet coincides with the larger scale baroclinic anticyclonic wave breaking associated with the polar jet (Figure 2a). The result is a deformation zone within the cyclone's warm conveyor belt system with two plumes of IVT making landfall in northern and southern California. Dropsondes from aircraft observations (Figures 3c-e) and satellite-based microwave observations of IWV (Wimmer & Velden, 2010; Supplementary Figure 1) further highlight the differing IWV and moisture transport characteristics of the IVT plumes. Both plumes demonstrated elevated moisture fluxes deep into the mid-troposphere (850-700 hPa; Figures 3c-e; Kaplan et al., 2012), with the deeper moisture in the southerly plume being transported from the tropics poleward by a northeastward-moving Kona Low (Morrison & Businger, 2001).

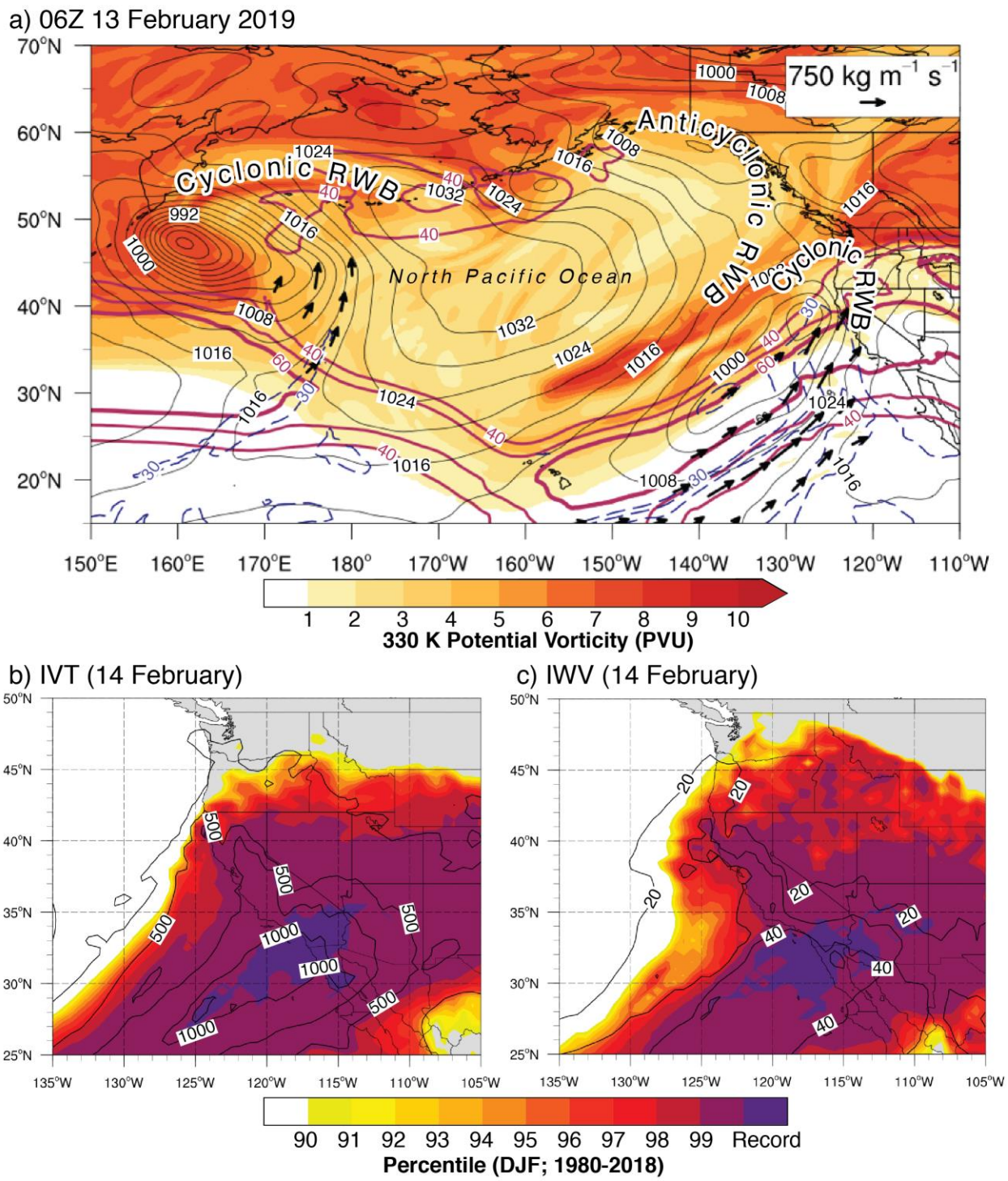

Figure 2: Large scale atmospheric conditions over the North Pacific Ocean and western North America at 06Z 13 February 2019 from the 0.5° Global Forecast System final analysis. Shown in (a) are: 330 K Isentropic Potential Vorticity (PVU; filled contours), 200 hPa wind speed (solid maroon contour; m/s), sea-level pressure (solid black contour; hPa), integrated water vapor (IWV; dashed blue contour; mm), integrated water vapor transport (IVT) vector (plotted

according to reference vector in upper right; kg m^{-1} s^{-1}); (b) Percentiles of 14 February 2019 IVT based upon 1980-2018 MERRA-2 winter (December-February) climatology (filled contours) and IVT values (black contours; kg m^{-1} s^{-1}); (c) As in (b) but for IWV (IWV contours have units of mm).

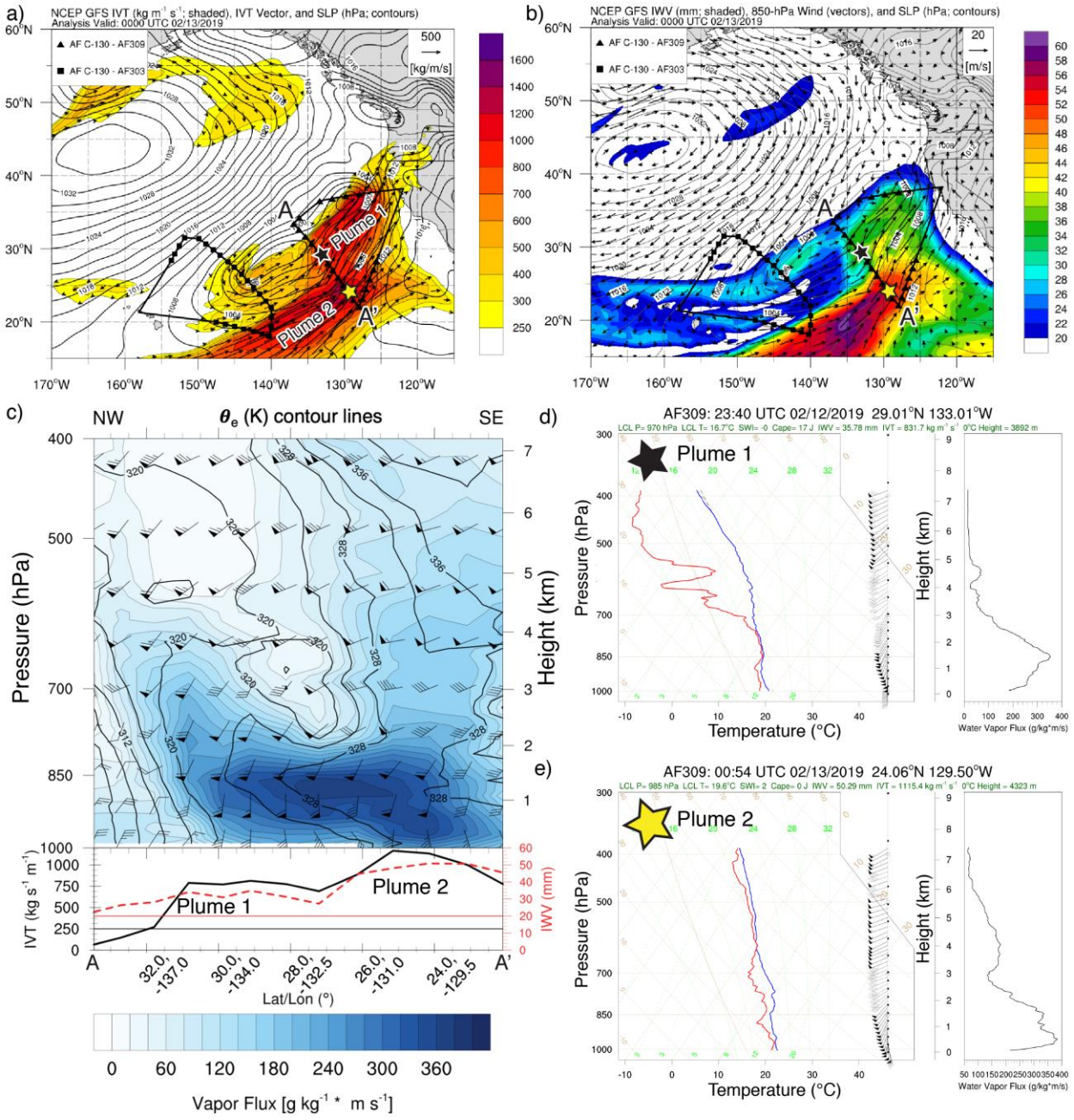

Figure 3: Model simulations and aircraft observations of the atmospheric river. (a) Global Forecast System simulated sea level pressure (open contours), integrated vapor transport (IVT; filled contours), and IVT vectors for 00Z 13 February 2019. (b) Global Forecast System simulated sea level pressure (open contours), integrated water vapor (IWV; filled contours), and

850 hPa wind vectors for 00Z 13 February 2019. (c) Dropsonde-derived vertical cross section over the two IVT plumes identified in (a). (d) Skew-T (left) and vertical profile of moisture fluxes (right) from the northern Plume 1 (black star). (e) As in (d) but for the southern Plume 2 (yellow star).

4 Record Southern California atmospheric moisture

The GNSS/GPS network observed integrated water vapor (IWV) exceeding 30 mm throughout Southern California on Valentine's Day (Figure 4), with Point Loma observing 46 mm at 1715Z (Figure 5a). The IWV observation from the 1200Z 14 February 2019 radiosonde launched from Miramar, CA set a cool season (October-April) record at 42.7 mm. This value was supported by a 1500Z radiosonde launched at the SIO pier in La Jolla that observed 45.4 mm (Supplementary Figure 2) with offshore dropsonde IWV observations exceeding 50 mm (Figure 3c). The extreme IVT and IWV (Figure 2b-c) combined with larger-scale dynamics (Figure 2a) to create an environment conducive to orographically-enhanced extreme rainfall (Ralph et al., 2013) with mountain precipitation corresponding to elevated upslope water vapor flux (Neiman et al., 2009; Figures 5b-d). The National Weather Service Cooperative Observer rain gauge at Palomar Observatory (elevation of 1,702 m), in northern San Diego County, measured 256 mm of rainfall in 24 hours, the highest 24-hour total since record keeping began in 1943. A co-located, sub-hourly ALERT gauge observed a similar total with periods of intense rainfall (Figure 5c). Many mountain regions in southern California observed rain rates exceeding United States Geological Survey general guidance for 15-minute intensity-duration thresholds for triggering post-fire debris flows (ranging between 12.5 and 21.8 mm hr^{-1}; Cannon et al., 2008; Staley et al., 2017). Hyperconcentrated flows and alluvial fan flash floods were observed in recently burned regions such as the Holy Fire (Figure 4) where 12-hour precipitation totals exceeded the 200-year return interval causing widespread flash flood impacts. The extreme precipitation at Snow Valley (Figure 5b) combined with snow levels exceeding 3 km (Figures 4 and 5b) resulted in full-path avalanches in the San Gorgonio Mountains and numerous landslides in the San Gabriel Mountains, including one that closed a 30 km segment of the Angeles Crest Highway for eight months (Burgess et al., 2019; Figure 4).

To characterize land surface conditions before and after this event, we examined the soil moisture conditions during the event using data from the University of California Los Angeles drought monitor (available at http://www.hydro.ucla.edu/SurfaceWaterGroup/forecast/monitor_ca/index.html; Mao et al., 2015; Xiao et al., 2017). Soil moisture in the drought monitor is reconstructed by the VIC model (Bohn et al., 2013). Precipitation fell on soils nearing saturation throughout Southern California. Prior to the event, soils were in the upper quartile of modeled soil moisture percentiles relative to the 1920-2010 climatology of the VIC model (Figures 1b and 4). These conditions favored runoff generation in both the uplands and lowlands. Ephemeral washes in the Palm Springs Desert observed the greatest flows since records began in 1987 (Figure 4), including a debris flow in Chino Canyon that damaged the Palm Springs Aerial Tramway (Desert Sun, 2019). Peak flows along inland-draining rivers with longer periods of record were notable. For example, the Mojave River (Figure 4) reached the top 0.2% of flows since observations began in 1930. Many ocean-draining and urbanized rivers also achieved flow rates that exceeded the top 1% of flow rates on record (Figure 4). It is worth noting rainfall-triggered mass movements were not

confined to southern California; landslides were documented in the San Francisco Bay area (Collins & Corbett, 2019) and in the western foothills of the Sierra Nevada.

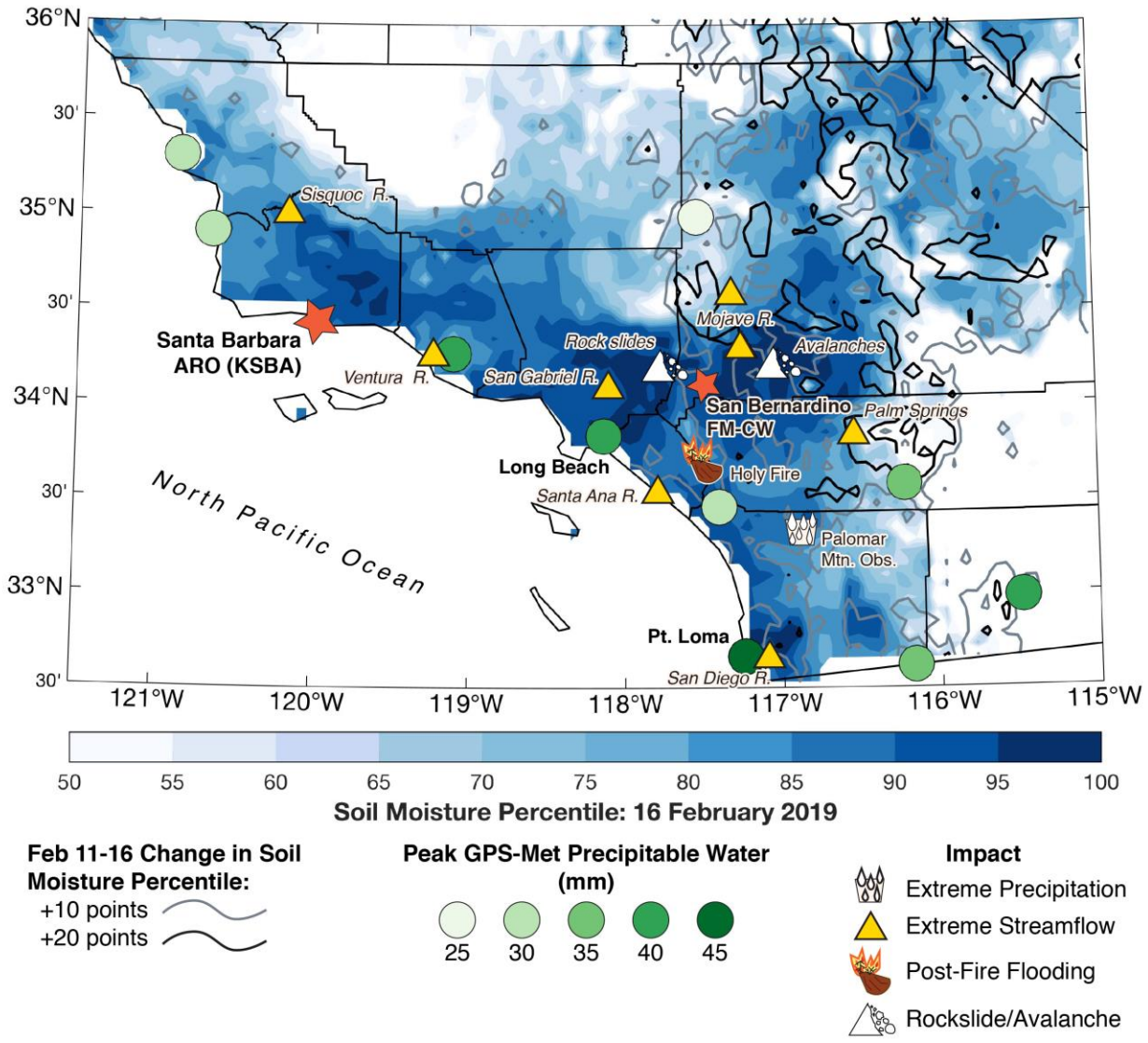

Figure 4: VIC-estimated soil moisture percentiles in Southern California on 16 February 2019 (filled contours) and soil moisture percentile changes between 12 and 16 February 2019 (open contours). Colored dots indicate peak event integrated water vapor (IWV) at GNSS/GPS sensors. Icons denote observed impacts and red stars indicate observation locations.

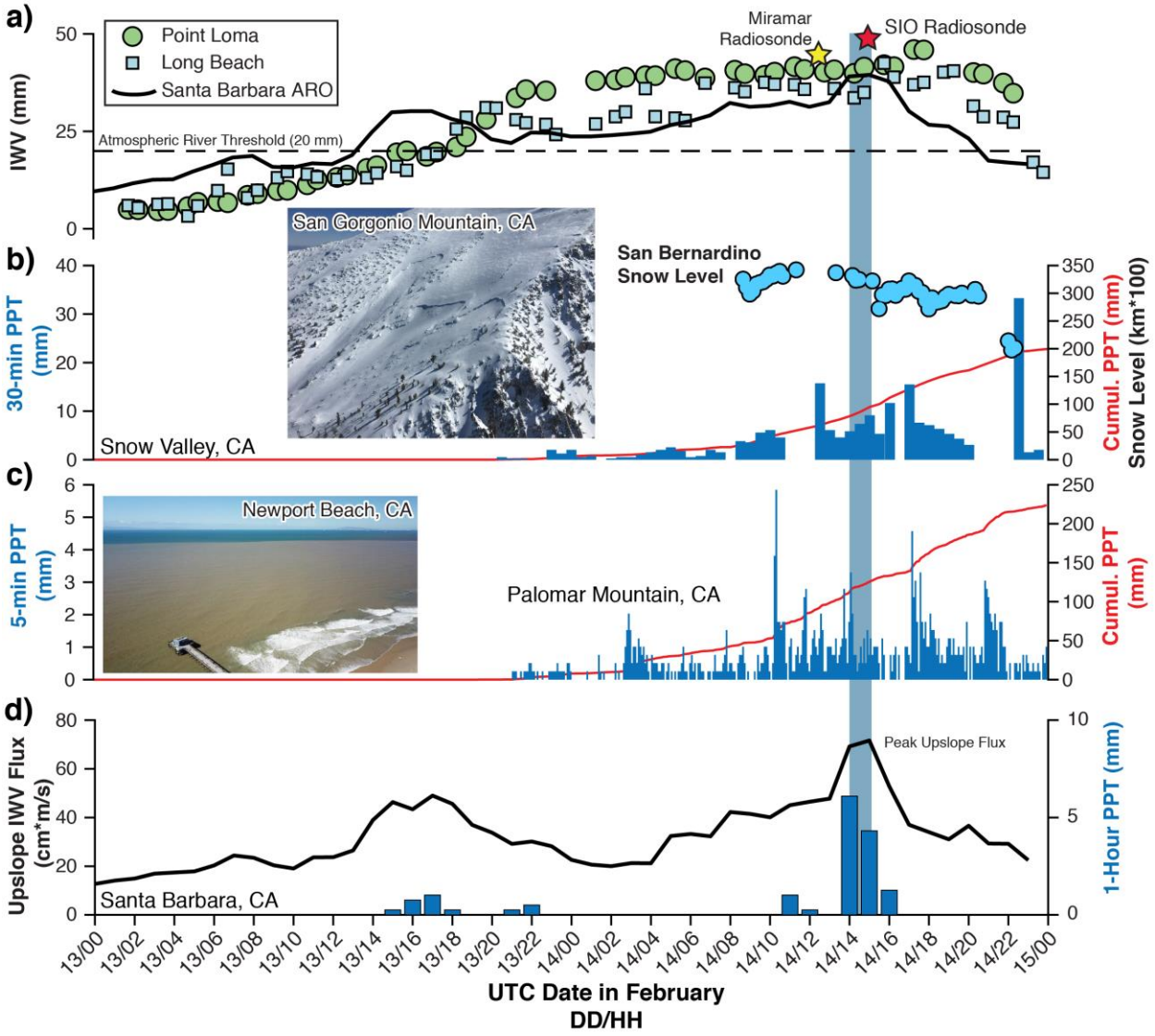

Figure 5: Southern California observations during 13-15 February 2019. (a) Time series of GNSS/GPS-derived IWV at Point Loma, Long Beach, and the Santa Barbara Atmospheric River Observatory (ARO). (b) Sub-hourly precipitation at Snow Valley ALERT gauge (blue bars) and cumulative precipitation (red line) with San Bernardino snow levels (blue dots). Image of the Mt. San Gorgonio avalanches (photo credit: Mike Nobriga via the So Cal Avalanche Center (http://www.socalsnow.org/avalanche-report-2-19-19-san-gorgonio.html). (c) As in (b) but for Palomar Mountain ALERT gauge. Newport Beach photograph provided by Royce Hurtain. (d) Upslope integrated water vapor flux derived from IWV and vertical wind profile at the Santa Barbara ARO. The shaded bar denotes the approximate time frame of the peak upslope water vapor flux.

5. Observations and impacts in California's Sierra Nevada and Southern Cascades

5.1 Snow level variability

Abrupt changes in snow level often accompany winter storms (White et al., 2019). Rises in snow level correspond to increases in streamflow as the advection of warm, moist air facilitates snowmelt and a growing fraction of the watershed receives rainfall (White et al., 2010; Hatchett et al., 2016; Hatchett, 2018). Snow level oscillations exceeding 1000 m and exceeding durations of 30 minutes were observed in the Sierra Nevada, with the ultimate snow level rise progressing from south to north (Figure 6). The varied timing and duration of these oscillations indicates mesoscale variability in snow level conditions throughout the Sierra Nevada (Minder et al., 2011; Minder & Kingsmill, 2013). Operational weather models have difficulty simulating variable situations, as demonstrated in the suite of California-Nevada River Forecast Center (CNRFC) freezing level forecasts (Figures 6c-d). Although some CNRFC ensemble members correctly approximate snow level rise timing and magnitude (Figures 6a-b), many estimate the snow level to be more than 1000 m lower than the level observed by the radar. This bias may lead to errors in streamflow forecasts (e.g., White et al., 2010).

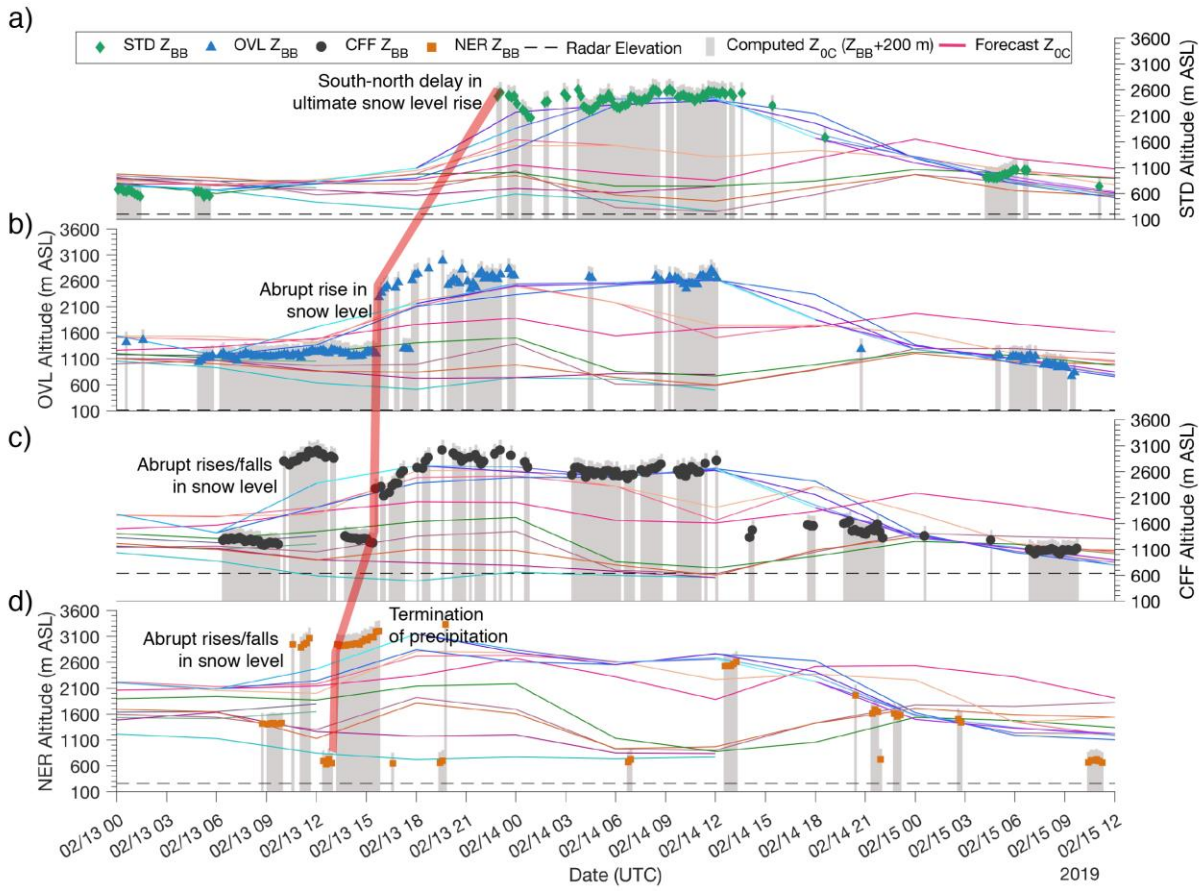

Figure 6: Snow level oscillations and freezing level forecasts. Time series of snow levels at (a) Shasta Dam (STD), (b) Oroville (OVL), (c) Colfax (CFF), and (d) New Exchequer (NER) snow level radar brightband heights (shown as symbols for each site), CNRFC freezing level forecasts (colored lines), freezing level based on radar brightband heights (computed by adding 200 m to each brightband value to account for the typical vertical distance between freezing level and snow level; Lundquist et al., 2008; White et al., 2010) for the period spanning 00Z 13 February-12Z 15 February 2019. Each radar location's elevation is shown as a dashed black line.

Expressing snow levels as percentiles provides another perspective of the magnitude of snow level variability during this event (Figure 7). Percentiles are calculated using 10-minute data for the December-February period over the respective periods of record for each radar (>5 years). Consistent with near-freezing temperatures at Shasta Dam (Figure 8a), low snow levels (bottom 10^{th} percentile) were observed before rising into the upper 15^{th} percentile. The lack of brightband observations (Figure 8b) despite precipitation observations (Figure 8c) is due to the brightband elevation being below the radar site. In the northern and central Sierra, snow level oscillations occurred between the upper and lower quartiles at Oroville, Colfax, and New Exchequer (Figure 7) leading to varying snowpack responses with elevation (Figures 8e-f). In the central Sierra Nevada, the lower elevation Blue Canyon and Greek Store snow pillows showed snow depth decreases throughout the event whereas depth increased at Mount Rose, a higher elevation station (Figure 8e). Snow water equivalent increased at all stations except Blue Canyon (Figure 8f). The increased streamflow following the snow level oscillation was realized at the Middle Forks of the American and Cosumnes River (Figure 8h) at approximately 1600Z 13 February 2019 and 0000Z 14 February 2019, respectively.

Snow level observations in the southern Sierra Nevada showed different responses than those in the north. Sporadic observations between 1300-1800Z 13 February 2019 at Pine Flat Dam and Kernville demonstrate the transition region between the northern and southern IVT plumes (Section 4; Figures 3a-b). We interpret these observations as representing the equatorward boundary of the initial wave of precipitation associated with the northern moisture plume (Figure 3). The southern moisture plume is characterized by high (top 10^{th} percentile) snow levels throughout its duration at Kernville and San Bernardino, consistent with 0°C elevations exceeding 4000 m observed in offshore dropsonde measurements (Figure 3e). Brightband observations at San Bernardino (located to the south of Kernville) began approximately six hours before Kernville and no brightband was observed further north until 20Z 14 February 2019 when cold frontal passage occurred (Figures 8a-b). This suggests the southern plume only impacted Southern California, and is consistent with the termination of precipitation at NER at 16Z 13 February (Figure 6d).

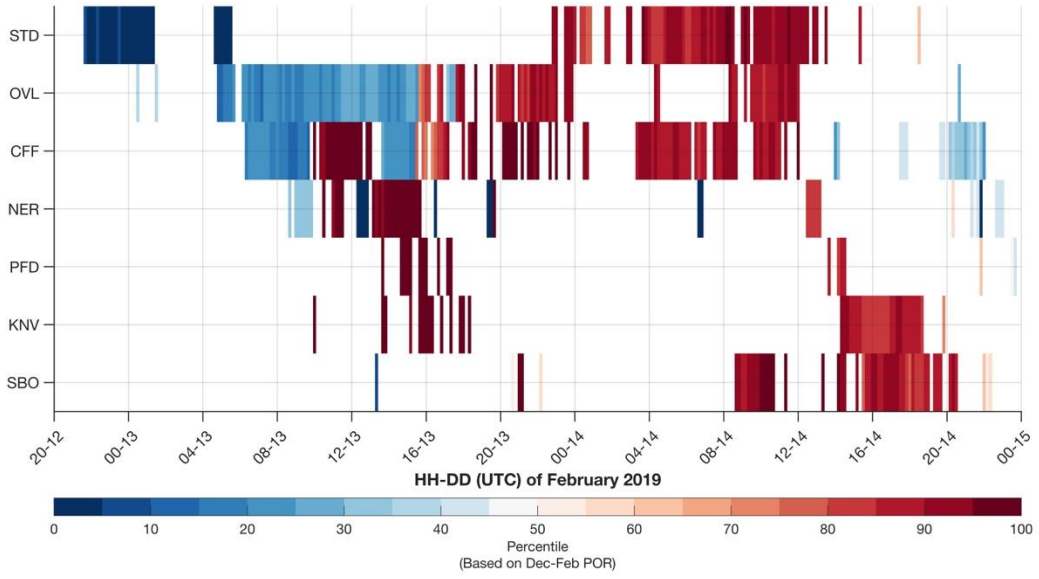

Figure 7: Ten-minute snow level percentiles for seven snow level radars in California spanning the period 20Z 12 February 2019-00Z 15 February 2019. Ordered from north to south: Shasta Dam (STD), Oroville (OVL), Colfax (CFF), New Exchequer (NER), Pine Flat Dam (PFD), Kernville (KNV), and San Bernardino (SBO).

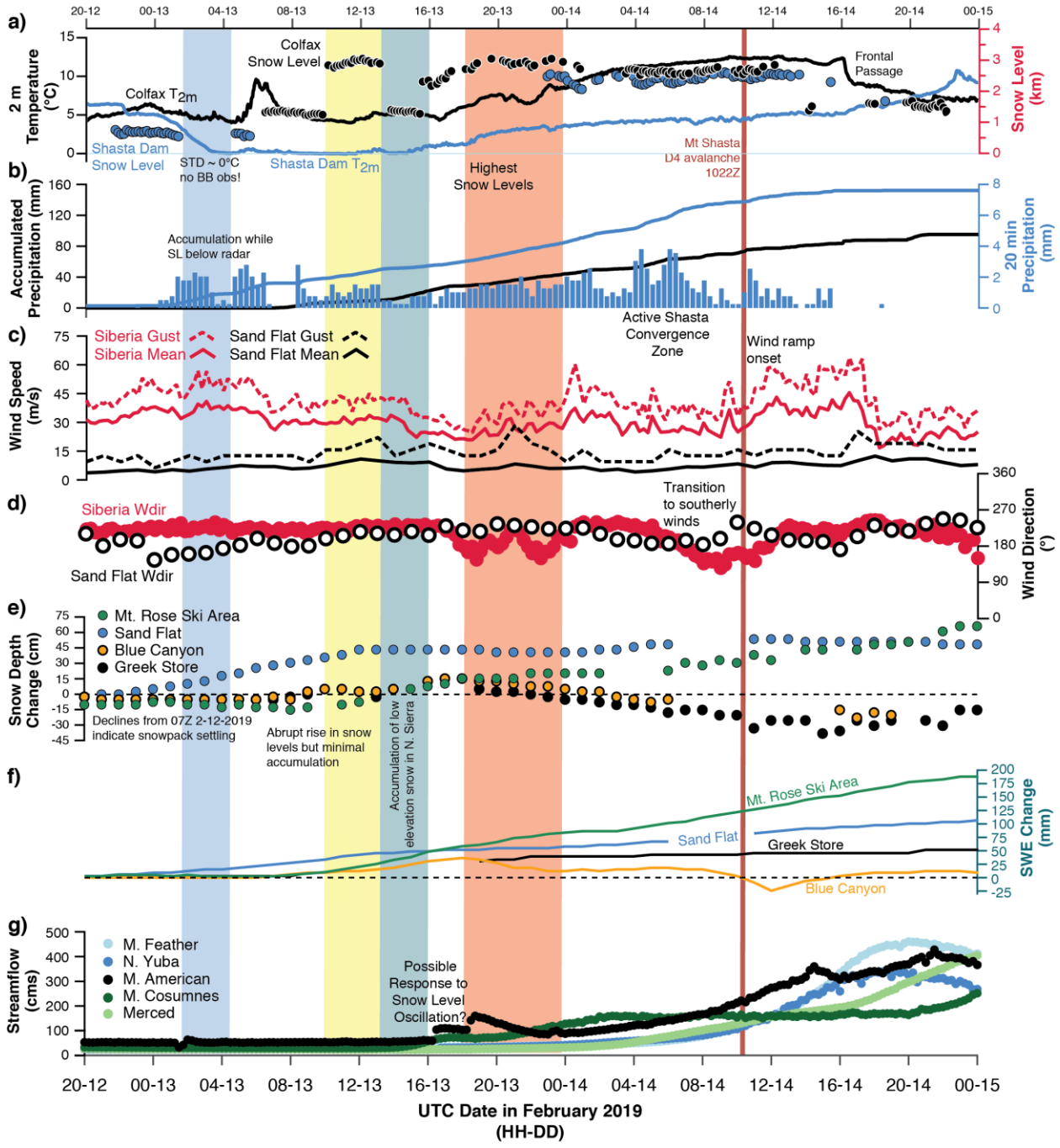

Figure 8: Time series of southern Cascades/northern Sierra Nevada observations from surface meteorological stations for the period spanning 20Z 12 February 2019-00Z 15 February 2019. (a) near-surface (2 m) temperature (left axis, solid lines) and snow level (right axis, points), (b) accumulated precipitation (left) and 20-minute precipitation (right), (c) wind speed, gust, and (d)

direction along the Sierra Nevada Crest (Siberia Ridge; in red) and south of Mt. Shasta (Grey Butte; black), (e) snow depth change, (f) snow water equivalent (SWE) change, and (g) streamflow.

5.2 Snow impacts on mountain transportation

During 13 February 2019, snow levels were among the lowest 5% of hourly observations during the past decade (2010-2019; Figure 7) at the Shasta Dam snow level radar site (elevation 202 m) before the brightband elevation fell below the station elevation (Figure 8b). Over 20 cm of snowfall was recorded in Redding, California (172 m), an uncommon occurrence in this area. Mount Shasta City (1000 m) recorded 60 cm of snowfall (Mount Shasta Avalanche Center (MSAC), 2019). This heavy low elevation snowfall slowed interstate commerce along Interstate 5 from the normal average of ~61,000 vehicles/day to ~24,000 vehicles (Caltrans, 2019). Traffic restrictions along Interstate 80 over the Sierra Nevada, a major east-west highway (average annual daily traffic of 35,000), began at 1800Z 13 February 2019 with a full closure from 0200Z 14 February 2019 to 0100Z 16 February 2019. Using average annual daily traffic volumes for each road with truck percentages of 12%, and a delay cost of $0.46/minute for trucks and $0.24/minute for cars (Caltrans, 2019), we estimate net commerce loss on the order of $21M during the Valentine's Day storm for these two major highways. This value represents a minimum estimate as delay costs for other impacted roads, such as Highway 50, and costs of repairs to damaged roads (e.g., Angeles Crest Highway; Section 4) are not included.

5.3 Mount Shasta avalanche timing and triggering

At approximately 1800Z 14 February 2019, evidence of a very large (R4/D4.5; Figures 9a-b) avalanche with a 5 km path length (Figure 9c) was discovered in the aptly-named Avalanche Gulch on the southwestern flank of Mount Shasta. Avalanche Gulch is a glacially sculpted canyon composed of steep sidewalls with numerous start zones at elevations between 3000-4000 m. Avalanche paths converge in the canyon bottom and terminate in gently sloping forested terrain 1000 m below. Depositional debris from this avalanche was approximately 10-20 m deep with 10 m tall flanks (Figure 9b). Avalanches of this magnitude on Mount Shasta are relatively rare, occurring on decadal scales (Hansen & Underwood, 2012).

The addition of over 80 mm of snow water equivalent (Figures 8b and 8e) is consistent with snowpack instability caused by continuous loading of new snow during atmospheric river events (Hatchett et al., 2017b). The MSAC advisory for 13 February was 'high', indicating naturally triggered large avalanches are likely. Synoptic conditions (Section 3) were consistent with those previously linked to large Mt. Shasta avalanche events (Hansen & Underwood, 2012).

Because no human observed the triggering or deposition time of the avalanche, we utilize the local seismic network (Figures 9c-e) to constrain the avalanche timing. The network recorded a high-energy spindle-like signal emerging from the background noise at 1022Z 14 February 2019 that lasted for ~2 minutes, followed by ~20 minutes of increased seismic energy. The waveforms observed at each station are broadband with frequencies ranging from 1-15 Hz and are dominated by energy between 2-5 Hz. These characteristics have been tied to avalanche activity by Kishimura & Izumi (1997). The signal duration (~2 min) and avalanche path length (5 km) yield an avalanche velocity of 42 m/s, consistent with dry or mixed slab avalanches (Vilajosana

et al., 2007). The two increases in energy within the wavetrain (Figure 8d) suggest distinct pulses in the avalanche process. Potential cultural origins of the seismic signal, notably train operations, were ruled out via spectral analysis and a second, smaller avalanche possibly occurred at 1740Z 14 February 2019.

Constraining the avalanche timing provides additional insight into potential triggering mechanisms. The avalanche occurred many hours after snow levels rose (Figure 8a), however the "upside-down" nature of the snowpack (more dense snow deposited atop less dense snow) inferred from lower snow levels followed by high snow levels (section 5.1) favors snowpack instability. H Regional winds (Figure 8c) and the Oroville and Twitchell Island wind profilers (Supplementary Figure 3) indicate accelerations in low-level (2-4 km; ~850–700 hPa) winds to 25 m/s at 0400Z 14 February with a turning of upper level winds to a more southeasterly direction (Figure 8d). These winds are reminiscent of the Sierra Nevada barrier jet that enhances northward moisture flux in the Central Valley (Parish, 1987; Neiman et al., 2002), increases precipitation in the northern Sierra Nevada and southern Cascades (Ralph et al., 2016), and helps establish the Shasta County Convergence Zone (Roberts, 2019; Figure 8b). Although the avalanche initiated on a southerly aspect normally scoured by prevailing southwesterly winds, deposition on this slope may have resulted from interactions of more southerly winds aloft (Figure 8d and Supplementary Figure 3) with Mt. Shasta. The low-level westerly flow at the Grey Butte (Figure 8d) station on the south flank of Mt. Shasta despite southerly flow aloft (Supplementary Figure 3) suggests airflow interactions with the mountain. Snow levels did not rise above 3 km (Figure 8a), rendering it unlikely that free-water introduction (Prowse & Owens, 1987) played a role in avalanche initiation in the start zone of Avalanche Gulch. In contrast, the San Gorgonio avalanches (Section 4) appeared to have occurred much closer in elevation (within 500 m) to the snow/rain transition level (Figure 5).

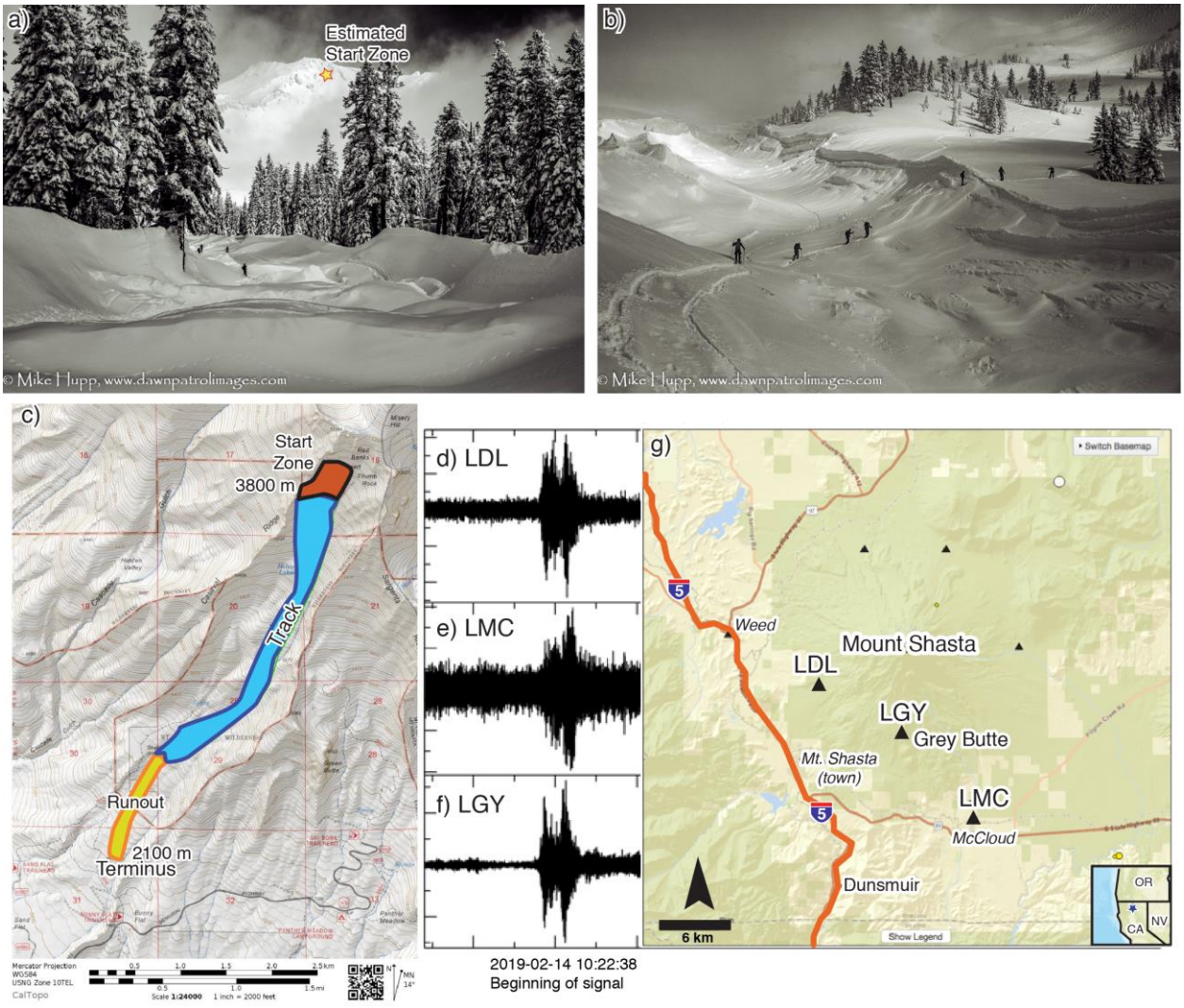

Figure 9: The Mt. Shasta avalanche. (a-b) Images of the avalanche from the runout zone (skiers for scale; images courtesy of Mike Hupp), c) Avalanche path map provided by the Mount Shasta Avalanche Center, d-f) Seismic signals from three seismometers located on the southwestern flank of Mount Shasta, g) location map of the seismic stations and the Grey Butte weather station.

6 Soil moisture improves Russian River streamflow forecasts

6.1 Hydrologic modeling approach

To provide a direct example of how observations from the Valentine's Day storm can be used for hydrologic modeling, we conducted an experiment applying the Distributed Hydrology Soil Vegetation Model (DHSVM; Wigmosta et al. 1994) to the Russian River watershed in northern California (Region III in Figure 1). The goal of the experiment is to examine the potential use of soil moisture sensors in model initialization and flood forecasting. We used the same model implementation as in Cao et al. (2019), in which calibration was performed for the period 2005-2014 at multiple stream gauges. We used 12 HMT soil moisture sites with at least three years of

data and included measurements during the Valentine's Day storm. The DHSVM as applied to the Russian River basin has three root zone soil layers with depths at 10 cm, 35 cm, and 75 cm.

We used the HMT measurements at depths of 10 cm, 15 cm, and 50 cm (the deepest measurement depth at most sites) as the corresponding model layers. In order to reconcile the soil moisture range difference in observations and the model, we converted both to hourly soil moisture percentiles relative to winter (November-March) 2017-2019 for each layer. We updated the model throughout the storm at a daily interval at midnight local time (0700Z). The observed soil moisture percentiles were interpolated over the basin using a Gaspari-Cohn function (Gaspari & Cohn, 1999) with a radius of 20 km where the weight decreased as the distance between an observation site and a target model grid cell increased (Figure 10a). We then interpolated the percentiles back to model values to update the soil moisture initialization state. We examined the effects of updating for the surface soil layer only, the upper two layers, and all three layers. We then explored the effects of this procedure at two USGS streamflow gages, the unimpaired upstream gage above Lake Mendocino (11461500; Figure 10a) and the downstream-most gage (11467000), which is influenced by reservoir operations at Lake Mendocino and Lake Sonoma (Figure 10a). We obtained the naturalized flows at the latter gage by calculating the difference of simulated streamflow with and without a reservoir module at this gauge and then adding the difference back to its observations, following Cao et al. (2019). We used the Kling-Gupta efficiency (KGE; Gupta et al., 2009) to evaluate the goodness-of-fit between hourly streamflow observations and hourly simulations at these two gages. KGE facilitates analysis of the various statistical components of the Nash-Sutcliffe efficiency, which is an objective method to evaluate runoff performance in hydrologic models.

6.2 Modeling Results

Soil moisture observations can provide information for situational awareness and model initialization on antecedent wetness conditions of a basin, a critical factor for flood forecasting (e.g., Brocca et al., 2010; Leroux et al., 2016; Zhang et al., 2016) as well as landslide forecasting (e.g., Godt et al., 2006; Thomas et al., 2018). Results showed that the KGE during the storm (0800Z 13 February 2019-0800Z 16 February 2019) increased from 0.19 to 0.42 by updating the surface layer, from 0.19 to 0.54 by updating the top two layers, and 0.19 to 0.66 by updating all three layers at the upstream USGS Gage 11461500. This heavily instrumented gage is surrounded by 7 out of 12 HMT sites in the Russian River watershed. Improvements increased as observations from deeper depths were included. However, the KGE at the downstream-most USGS Gage 1146700 did not increase with each additional depth. The KGE changed from 0.89 to 0.95, 0.90, and 0.70 respectively with updates of the uppermost layer only, upper two layers, and all three layers. This result is possibly due to the sparse distribution of the downstream HMT sites and the influence of historical calibration at different gauge locations. Although these results are for a single storm, they do have implications for placement of soil moisture stations and for the manner in which the updating is performed. These results suggest that flood forecasting is likely to benefit from both measurements at depths beyond the surface layer and a denser spatial distribution of soil moisture observations in the drainage area of interest. These measurements also support landslide hazard monitoring (Thomas et al., 2019).

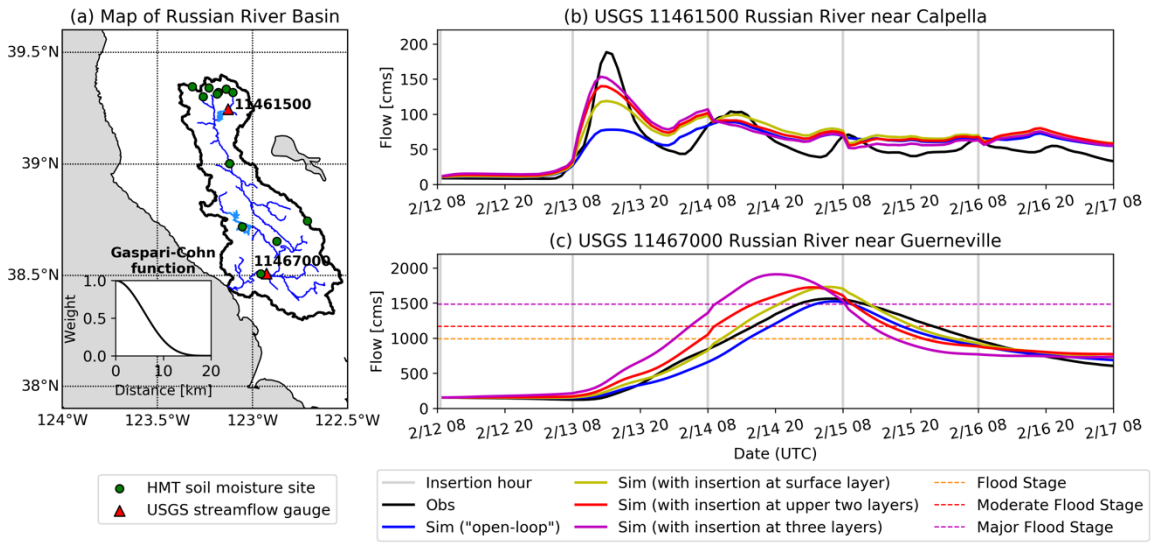

Figure 10: Hydrologic modeling results from the Russian River watershed. a) Map of the Russian River watershed, with locations of USGS stream gauges and Hydrometeorology Testbed (HMT) soil moisture observation sites shown. Observed and simulated hourly streamflow time series during the Valentine's day storm at upstream USGS Gauges (b) 11461500 and (c) 11467000. Gauge 11467000 is impacted by reservoir operations at Lake Mendocino and Lake Sonoma, the effect of which has been removed in the observed streamflow time series shown.

7 Discussion

Atmospheric rivers commonly drive extreme hydrometeorological events and hydroclimate variability worldwide (Paltan et al., 2017). Data provided by California's diverse observational network facilitates development of conceptual linkages between natural hazards and meteorological or hydrological precursor and triggering conditions during atmospheric river conditions. These linkages are deepened by incorporating other observational networks, such as the GNSS/GPS network (Moore et al., 2015) and ALERT gauges (Section 4) or seismic networks (Section 5.3). The rise in soil moisture to the upper quartile following the event (Figures 1b-c and 4a) indicates steepland regions were more likely to produce runoff if closely followed by additional precipitation events, leading to continued natural hazard risks from flooding (Cao et al., 2019) and mass wasting (Oakley et al., 2018b). In highly urbanized areas, like Southern California, extreme runoff (Figure 4) also degrades coastal water quality (Figure 5c inset) leading to beach closures and public health impacts (Aguilera et al., 2019) in addition to localized flooding.

Our examination of the 2019 Valentine's Day storm, using a subset of data from a multi-tiered observational network and augmented with additional sources of information, illustrates how these networks help characterize physical processes and their impacts. This effort, as well as other work utilizing data from the network (e.g., Martin et al., 2018; Ralph et al., 2013; Sterle et al., 2019; Wang et al., 2019; White et al., 2019), indicates the network is achieving the goals outlined in White et al. (2013) and Ralph et al. (2014). These goals include providing information regarding real-time monitoring, hydrologic prediction from minutes to seasons, data

assimilation, research applications leading to physical process understanding and model limitations, and climate trend analysis (Ralph et al. 2014).

The high temporal resolution of the network and diverse data sources (e.g., aircraft and *in-situ*) allowed observations of processes that would otherwise go un-verified, such as the record precipitable water in southern California (Section 4) or un-reported, like the dramatic oscillations in snow level (Section 5.1). Soil moisture observations were demonstrated to improve hydrologic model output (Section 6). Multi-tiered observations, such as aircraft-based atmospheric river reconnaissance, use targeting strategies to optimize mission-based observations of key weather phenomena over the data-sparse North Pacific Ocean to support numerical weather prediction efforts and supplement interpretations of impacts (Martin et al., 2018; Sections 4-5). These efforts can be used to identify weaknesses in numerical model output, an example being the case of the CNRFC freezing level forecasts (Section 5.1).

In other challenging forecast scenarios, such as low or varying snow levels (Sections 5.1-5.2), model validation is performed in real-time at coastal Atmospheric River Observatories (AROs; Supplementary Figure 4) and at snow level radar sites (Supplementary Figure 5; Ray & White, 2019). AROs combine numerous observations with short-term high-resolution model simulations to enhance short-term forecasting for these situations. This combination is colloquially known as the "Integrated Water Vapor Flux Tool" (Neiman et al., 2009; Supplementary Figure 4). First used in conjunction with rapidly updating forecast models (White et al., 2012), this tool now exists with multiple operational and research versions of weather models (cf. Figure 2 in Ray & White, 2019). The tool provides a recent history of key parameters associated with observed AR-related features such as upslope water vapor flux, precipitation, and recent model forecast performance. This information can influence forecaster confidence regarding the next 12-hr forecast period and impact-based decision support (Uccellini & Ten Hoeve, 2019) on issuing or extending weather-related warnings based on whether or not heavy precipitation is forecast to continue. We recommend model forecasts and recent verification statistics be expanded to all suites of instruments, such as the GNSS/GPS sensors and snow pillows, especially as modeling capabilities move towards ensemble-based, probabilistic forecasts (e.g., National Blend of Models; Hammil et al., 2017). Discovering model weaknesses in reproducing observed phenomena motivates targeted improvements in forecast skill (e.g., Olson et al., 2019) leading to enhanced public and emergency management preparedness and response during, and following, extreme events.

Capturing snow and freezing level oscillations (Section 5.1) in operational runoff models is one example of the need for improved forecasts and process-based understanding for water management, a key aim of a multi-tiered observational network (White et al., 2013; Ralph et al., 2014). Snow level variability at the mountain range scale, especially when considerable model spread exists (Figure 6), means the water conveyance system must be managed between different operator groups to ensure release needs can be met with minimal downstream flood impacts and keeping within operational constraints of reservoir levels (White et al., 2010; Talbot et al., 2019). Our analysis of the impact of the snow level oscillations and streamflow responses in the northern Sierra Nevada (Figure 8) is limited by the daily resolution of upstream reservoir storage data at the Hell Hole and Frenchman's reservoirs on the Middle Fork of the American River. This indicates the need for additional sub-daily observations of soil moisture and streamflow on both impaired and unimpaired river basins to precisely evaluate physical drivers of hydrologic

responses and to calibrate model simulations aimed at reproducing these responses. Such information could provide additional early warning for landslide hazards (Section 4).

Improving the real-time accessibility of observational data from diverse networks will facilitate applying the data towards broader goals of achieving water supply resilience, flood risk management, and the understanding of and resiliency to other extreme events such as mass movement, wildfire, and heat extremes. The increasing exposure of life and property to natural hazards amidst climate change and population growth creates opportunities for integrated observational networks to support long-term management goals (Lundquist et al., 2016). These networks contribute towards a baseline understanding of current hydroclimate conditions, how different environments respond to extreme events under varying antecedent conditions, and how well forecast models perform when initialized with differing initial and boundary conditions. The complexity of natural systems presents a challenge for quickly characterizing the range of possible outcomes from a given extreme event. In the case of California's network, many of these observations have been collected over varied antecedent conditions in the past decade that can be placed into the context of past extreme climate conditions over longer timescales (e.g., Hatchett et al., 2018; Sterle et al., 2019). This confidence to understand potential outcomes allows focused efforts on mitigating impacts, a key goal of decision support (Uccellini & Ten Hoeve, 2019).

8 Concluding Remarks

California's multi-tiered network of diverse observations provides real-time information pertinent to the analysis of extreme events throughout the state. These observations can help characterize the triggering mechanisms and impacts of natural hazards. This makes natural hazard risk mitigation more achievable through improvements in forecasting and decision support aimed at timely resource positioning for effective emergency response. Our goal was to explore and illustrate the utility of this unique network in understanding physical origins of impacts that occurred during the 2019 Valentine's Day winter storm. We conclude that California's observational network is successfully implementing ideas that emerged from many agency planning efforts (summarized in Ralph et al., 2014) and of testing and demonstration carried out through the NOAA Hydrometeorology Testbed (White et al., 2012; Ralph et al., 2013).

Components of the network with many years of observations, such as snow level radar, soil moisture, or GPS, can now be used to place extreme events into climatological context and establish a baseline state of regional hydroclimate conditions (e.g., Hatchett et al., 2017a; Cao et al., 2019; Sterle et al., 2019). By helping identify drivers of hydrometeorological impacts in sensitive ecosystems or on values-at-risk, the network helps prioritize future investments and studies aimed at mitigating risks and enhancing the resiliency of water resources at local and regional scales (White et al., 2013; Ralph et al., 2014). Continued investments towards establishing and maintaining what are now becoming long-term observational networks will be critical to understand how natural systems are evolving (e.g., Mensing et al., 2013; Lundquist et al., 2016). Multi-tiered observing and forecast systems should be further integrated with data display to better serve multiple agencies with different but overlapping missions (e.g., https://cw3e.ucsd.edu/DSMaps/DS_intro.html). Process-based understanding and subsequent improvements in forecast confidence at longer lead times will translate towards better decision

support during events and inform longer-term shifts to the water management landscape. With future weather and climate extremes projected to increase in the western U.S. (Gershunov et al., 2019), continuing to collect and utilize observations from California's network will help improve early warning and emergency response times during these events.

Acknowledgments and Data

This work was supported by the California Department of Water Resources under agreement Atmospheric Rivers Program DWR-4600010378 TO#15 Am 22. The authors declare no conflicts of interest. All data is publicly available from the locations listed in Table 1 and the repositories noted in data reference. Seismic waveform data, metadata, or data products for this study were accessed through the Northern California Earthquake Data Center (NCEDC), doi:10.7932/NCEDC. We thank Royce Hurtain (@visual_burrito), Mike Nobriga and the So Cal Avalanche Center (http://www.socalsnow.org/), and Mike Hupp (http://www.dawnpatrolimages.com) for photographs of storm impacts.

References

Abatzoglou, J. T. (2013). Development of gridded surface meteorological data for ecological applications and modelling. *International Journal of Climatology*, *33*(1), 121-131. https://doi.org/10.1002/joc.3413

Abatzoglou, J. T., & Magnusdottir, G. (2006). Planetary wave breaking and nonlinear reflection: Seasonal cycle and interannual variability. *Journal of Climate*, *19*(23), 6139-6152. https://doi.org/10.1175/JCLI3968.1

Aguilera, R., Gershunov, A., & Benmarhnia, T. (2019). Atmospheric rivers impact California's coastal water quality via extreme precipitation. *Science of The Total Environment*, *671*, 488-494. https://doi.org/10.1016/j.scitotenv.2019.03.318

Bevis, M., Businger, S., Herring, T. A., Rocken, C., Anthes, R. A., & Ware, R. H. (1992). GPS meteorology: Remote sensing of atmospheric water vapor using the Global Positioning System. *Journal of Geophysical Research: Atmospheres*, *97*(D14), 15787-15801. https://doi.org/10.1029/92JD01517

Bohn, T. J., B. Livneh, J. W. Oyler, S. W. Running, B. Nijssen, and D. P. Lettenmaier, 2013: Global evaluation of MTCLIM and related algorithms for forcing of ecological and hydrological models, *Agricultural and Forest Meteorology*, **176**, 38-49, https:/doi.org/10.1016/j.agrformet.2013.03.003

Brocca, L., Melone, F., Moramarco, T., Wagner, W., Naeimi, V., Bartalis, Z., & Hasenauer, S. (2010). Improving runoff prediction through the assimilation of the ASCAT soil moisture product. *Hydrology and Earth System Sciences*, *14*(10), 1881-1893. https://doi.org/10.5194/hess-14-1881-2010

Burgess, W.P., Beard, R.A., Lancaster, J.T., and Wurgler R.A. (2019). California Recent Reported Landslide Map: http://maps.conservation.ca.gov/cgs/lsi/app/

California Department of Transportation (Caltrans). (2019). Public Records Request: R003575-082019.

Cannon, S. H., Gartner, J. E., Wilson, R. C., Bowers, J. C., & Laber, J. L. (2008). Storm rainfall conditions for floods and debris flows from recently burned areas in southwestern Colorado and southern California. *Geomorphology*, *96*(3-4), 250-269. https://doi.org/10.1016/j.geomorph.2007.03.019

Cayan, D. R., Dettinger, M. D., Pierce, D., Das, T., Knowles, N., Ralph, F. M., & Sumargo, E. (2016). Natural variability, anthropogenic climate change, and impacts on water availability and flood extremes in the Western United States. *Water Policy and Planning in a Variable and Changing Climate*, *17*. https://doi.org/10.1201/b19534-4

Cifelli, R., Chandrasekar, V., Chen, H., & Johnson, L. E. (2018). High resolution radar quantitative precipitation estimation in the San Francisco Bay area: rainfall monitoring for the urban environment. *Journal of the Meteorological Society of Japan. Ser. II*, *96*, 141-155. https://doi.org/10.2151/jmsj.2018-016

Cordeira, J. M., Ralph, F. M., Martin, A., Gaggini, N., Spackman, J. R., Neiman, P. J., ... & Pierce, R. (2017). Forecasting atmospheric rivers during CalWater 2015. *Bulletin of the American Meteorological Society*, *98*(3), 449-459. https://doi.org/10.1175/BAMS-D-15-00245.1

Corringham, T. W., Ralph, F. M., Gershunov, A., Cayan, D. R., & Talbot, C. A. (2019). Atmospheric rivers drive flood damages in the western United States. *Science Advances*, *5*(12), eaax4631. https://doi.org/10.1126/sciadv.aax4631

Desert Sun. (2019). Palm Springs declares local emergency after flooding causes nearly $1.9 million in damage. Available at: [https://www.desertsun.com/story/news/local/palm-springs/2019/03/07/palm-springs-declares-emergency-outlines-nearly-2-million-flood-damage/3087113002/]

Dettinger, M. D., Ralph, F. M., Das, T., Neiman, P. J., & Cayan, D. R. (2011). Atmospheric rivers, floods and the water resources of California. *Water*, *3*(2), 445-478. https://doi.org/10.3390/w3020445

Environmental Modeling Center. (2003). The GFS Atmospheric Model. NOAA/NCEP/Environmental Modeling Center Office Note 442, 14 pp. [Available online at http://www.emc.ncep.noaa.gov/officenotes/FullTOC.html].

Gaspari, G., & Cohn, S. E. (1999). Construction of correlation functions in two and three dimensions. *Quarterly Journal of the Royal Meteorological Society*, *125*(554), 723-757. https://doi.org/10.1002/qj.49712555417

Gelaro, R., McCarty, W., Suárez, M. J., Todling, R., Molod, A., Takacs, L., et al. (2017). The modern-era retrospective analysis for research and applications, version 2 (MERRA-2). *Journal of Climate*, *30*(14), 5419-5454. https://doi.org/10.1175/JCLI-D-16-0758.1

Gershunov, A., Shulgina, T., Clemesha, R. E., Guirguis, K., Pierce, D. W., Dettinger, M. D., et al. (2019). Precipitation regime change in Western North America: the role of Atmospheric Rivers. *Scientific Reports*, *9*(1), 1-11. https://doi.org/10.1038/s41598-019-46169-w

Gupta, H. V., Kling, H., Yilmaz, K. K., & Martinez, G. F. (2009). Decomposition of the mean squared error and NSE performance criteria: Implications for improving hydrological modelling. *Journal of Hydrology*, *377*(1-2), 80-91. https://doi.org/10.1016/j.jhydrol.2009.08.003

Hamill, T. M., Engle, E., Myrick, D., Peroutka, M., Finan, C., & Scheuerer, M. (2017). The US National Blend of Models for statistical postprocessing of probability of precipitation and deterministic precipitation amount. *Monthly Weather Review*, *145*(9), 3441-3463. https://doi.org/10.1175/MWR-D-16-0331.1

Hansen, C., & Underwood, S. J. (2012). Synoptic scale weather patterns and size-5 avalanches on Mt. Shasta, California. *Northwest Science*, *86*(4), 329-341. https://doi.org/10.3955/046.086.0408

Hatchett, B. (2018). Snow Level Characteristics and Impacts of a Spring Typhoon-Originating Atmospheric River in the Sierra Nevada, USA. *Atmosphere*, *9*(6), 233. https://doi.org/10.3390/atmos9060233

Hatchett, B. J., Kaplan, M. L., & Burak, S. (2016). Some characteristics of upside-down storms in the northern Sierra Nevada, California-Nevada, USA. *Proc. International Snow Science Workshop*, Breckenridge, CO. Available at: [http://arc.lib.montana.edu/snow-science/objects/ISSW16_P4.03.pdf]

Hatchett, B., Daudert, B., Garner, C., Oakley, N., Putnam, A., & White, A. (2017a). Winter snow level rise in the northern Sierra Nevada from 2008 to 2017. *Water*, *9*(11), 899. https://doi.org/10.3390/w9110899

Hatchett, B. J., Burak, S., Rutz, J. J., Oakley, N. S., Bair, E. H., & Kaplan, M. L. (2017b). Avalanche fatalities during atmospheric river events in the western United States. *Journal of Hydrometeorology*, *18*(5), 1359-1374. https://doi.org/10.1175/JHM-D-16-0219.1

Hatchett, B. J., Boyle, D. P., Garner, C. B., Kaplan, M. L., Bassett, S. D., & Putnam, A. E. (2018). Sensitivity of a western Great Basin terminal lake to winter northeast Pacific storm track activity and moisture transport. *Geol. Soc. Am. Spec. Papers*, *536*, 67-79. https://doi.org/10.1130/2018.2536(05)

Hu, H., Dominguez, F., Wang, Z., Lavers, D. A., Zhang, G., & Ralph, F. M. (2017). Linking atmospheric river hydrological impacts on the US West Coast to Rossby wave breaking. *Journal of Climate*, *30*(9), 3381-3399. https://doi.org/10.1175/JCLI-D-16-0386.1

Johnston, P. E., Jordan, J. R., White, A. B., Carter, D. A., Costa, D. M., & Ayers, T. E. (2017). The NOAA FM-CW snow-level radar. *Journal of Atmospheric and Oceanic Technology*, *34*(2), 249-267. https://doi.org/10.1175/JTECH-D-16-0063.1

Kaplan, M. L., Vellore, R. K., Marzette, P. J., & Lewis, J. M. (2012). The role of windward-side diabatic heating in Sierra Nevada spillover precipitation. *Journal of Hydrometeorology*, *13*(4), 1172-1194. https://doi.org/10.1175/JHM-D-11-06.1

Kishimura, K., & Izumi, K. (1997). Seismic signals induced by snow avalanche flow. *Natural Hazards*, *15*(1), 89-100. https://doi.org/10.1023/A:1007934815584

Lamjiri, M. A., Dettinger, M. D., Ralph, F. M., & Guan, B. (2017). Hourly storm characteristics along the US West Coast: Role of atmospheric rivers in extreme precipitation. *Geophysical Research Letters*, *44*(13), 7020-7028. https://doi.org/10.1002/2017GL074193

Leroux, D. J., Pellarin, T., Vischel, T., Cohard, J. M., Gascon, T., Gibon, F., et al. (2016). Assimilation of SMOS soil moisture into a distributed hydrological model and impacts on the water cycle variables over the Ouémé catchment in Benin. *Hydrology and Earth System Sciences*, *20*(7), 2827-2840. https://doi.org/10.5194/hess-20-2827-2016

Liang, X., Lettenmaier, D. P., Wood, E. F., & Burges, S. J. (1994). A simple hydrologically based model of land surface water and energy fluxes for general circulation models. *Journal of Geophysical Research: Atmospheres*, *99*(D7), 14415-14428. https://doi.org/10.1029/94JD00483

Liu, Q. H., & Weng, F. Z. (2005). One-Dimensional Variational Retrieval Algorithm of Temperature, Water Vapor, and Cloud Water Profiles from Advanced Microwave Sounding Unit (AMSU). *IEEE Transactions on Geoscience and Remote Sensing*, 43(5), 1087-1095. https://doi.org/10.1109/TGRS.2004.843211

Lundquist, J. D., & Cayan, D. R. (2007). Surface temperature patterns in complex terrain: Daily variations and long-term change in the central Sierra Nevada, California. *Journal of Geophysical Research: Atmospheres*, *112*(D11). https://doi.org/10.1029/2006JD007561

Lundquist, J. D., Neiman, P. J., Martner, B., White, A. B., Gottas, D. J., & Ralph, F. M. (2008). Rain versus snow in the Sierra Nevada, California: Comparing Doppler profiling radar and surface observations of melting level. *Journal of Hydrometeorology*, *9*(2), 194-211. https://doi.org/10.1175/2007JHM853.1

Lundquist, J. D., Roche, J. W., Forrester, H., Moore, C., Keenan, E., Perry, G., ... & Cayan, D. R. (2016). Yosemite Hydroclimate Network: Distributed stream and atmospheric data for the Tuolumne River watershed and surroundings. *Water Resources Research*, *52*(9), 7478-7489. https://doi.org/10.1002/2016WR019261

Mao, Y., Nijssen, B., & Lettenmaier, D. P. (2015). Is climate change implicated in the 2013–2014 California drought? A hydrologic perspective. *Geophysical Research Letters*, *42*(8), 2805-2813. https://doi.org/10.1002/2015GL063456

Martin, A., Ralph, F. M., Demirdjian, R., DeHaan, L., Weihs, R., Helly, J., et al. (2018). Evaluation of Atmospheric River Predictions by the WRF Model Using Aircraft and Regional Mesonet Observations of Orographic Precipitation and Its Forcing. *Journal of Hydrometeorology*, *19*(7), 1097-1113. https://doi.org/10.1175/JHM-D-17-0098.1

Mensing, S., Strachan, S., Arnone, J., Fenstermaker, L., Biondi, F., Devitt, D., et al. (2013). A network for observing Great Basin climate change. *Eos, Transactions American Geophysical Union*, *94*(11), 105-106. https://doi.org/10.1002/2013EO110001

Minder, J. R., Durran, D. R., & Roe, G. H. (2011). Mesoscale controls on the mountainside snow line. *Journal of the Atmospheric Sciences*, *68*(9), 2107-2127. https://doi.org/10.1175/JAS-D-10-05006.1

Minder, J. R., & Kingsmill, D. E. (2013). Mesoscale variations of the atmospheric snow line over the northern Sierra Nevada: Multiyear statistics, case study, and mechanisms. *Journal of the Atmospheric Sciences*, *70*(3), 916-938. https://doi.org/10.1175/JAS-D-12-0194.1

Mount Shasta Avalanche Center. (2019). Mount Shasta Avalanche and Climbing Information. Accessed February 20, 2019. https://www.shastaavalanche.org/

Morrison, I. & Businger S. (2001). Synoptic structure and evolution of a Kona low. *Weather and Forecasting*, 16: 81– 98. https://doi.org/10.1175/1520-0434(2001)016<0081:SSAEOA>2.0.CO;2

Moore, A. W., Small, I. J., Gutman, S. I., Bock, Y., Dumas, J. L., Fang, P., et al. (2015). National Weather Service Forecasters use GPS precipitable water vapor for enhanced situational awareness during the Southern California Summer Monsoon. *Bulletin of the American Meteorological Society*, *96*(11), 1867-1877. https://doi.org/10.1175/BAMS-D-14-00095.1

Moore, B. J., Keyser, D., & Bosart, L. F. (2019). Linkages between Extreme Precipitation Events in the Central and Eastern United States and Rossby Wave Breaking. *Monthly Weather Review*, *147*(9), 3327-3349. https://doi.org/10.1175/MWR-D-19-0047.1

Nardi, K. M., Barnes, E. A., & Ralph, F. M. (2018). Assessment of numerical weather prediction model reforecasts of the occurrence, intensity, and location of atmospheric rivers along the West Coast of North America. *Monthly Weather Review*, *146*(10), 3343-3362. https://doi.org/10.1175/MWR-D-18-0060.1

Neiman, P. J., White, A. B., Ralph, F. M., Gottas, D. J., & Gutman, S. I. (2009, April). A water vapour flux tool for precipitation forecasting. In *Proceedings of the Institution of Civil Engineers-Water Management* (Vol. 162, No. 2, pp. 83-94). Thomas Telford Ltd. https://doi.org/10.1680/wama.2009.162.2.83

Northern California Earthquake Data Center (NCEDC) (2014). Northern California Earthquake Data Center. UC Berkeley Seismological Laboratory. Dataset. https://doi.org/10.7932/NCEDC

Oakley, N. S., Lancaster, J. T., Kaplan, M. L., & Ralph, F. M. (2017). Synoptic conditions associated with cool season post-fire debris flows in the Transverse Ranges of southern California. *Natural Hazards*, *88*(1), 327-354. https://doi.org/10.1007/s11069-017-2867-6.

Oakley, N. S., Cannon, F., Munroe, R., Lancaster, J. T., Gomberg, D., & Ralph, F. M. (2018a). Brief communication: Meteorological and climatological conditions associated with the 9 January 2018 post-fire debris flows in Montecito and Carpinteria, California, USA. *Natural Hazards and Earth System Sciences*, *18*(11), 3037-3043. https://doi.org/10.5194/nhess-18-3037-2018.

Oakley, N. S., Lancaster, J. T., Hatchett, B. J., Stock, J., Ralph, F. M., Roj, S., & Lukashov, S. (2018b). A 22-Year Climatology of Cool Season Hourly Precipitation Thresholds Conducive to Shallow Landslides in California. *Earth Interactions*, *22*(14), 1-35. https://doi.org/10.1175/EI-D-17-0029.1

Olson, J. B., Kenyon, J. S., Djalalova, I., Bianco, L., Turner, D. D., Pichugina, Y., et al. (2019). Improving wind energy forecasting through numerical weather prediction model development. In press, *Bulletin of the American Meteorological Society*. https://doi.org/10.1175/BAMS-D-18-0040.1

Paltan, H., Waliser, D., Lim, W. H., Guan, B., Yamazaki, D., Pant, R., & Dadson, S. (2017). Global floods and water availability driven by atmospheric rivers. *Geophysical Research Letters*, *44*(20), 10-387. https://doi.org/10.1002/2017GL074882

Payne, A. E., & Magnusdottir, G. (2014). Dynamics of landfalling atmospheric rivers over the North Pacific in 30 years of MERRA reanalysis. *Journal of Climate*, *27*(18), 7133-7150. https://doi.org/10.1175/JCLI-D-14-00034.1

Prowse, T. D., & Owens, I. F. (1984). Characteristics of snowfalls, snow metamorphism, and snowpack structure with implications for avalanching, Craigieburn Range, New Zealand. *Arctic and Alpine Research*, *16*(1), 107-118. https://doi.org/10.2307/1551176

Ralph, F. M., Rauber, R. M., Jewett, B. F., Kingsmill, D. E., Pisano, P., Pugner, P., et al. (2005). Improving short-term (0–48 h) cool-season quantitative precipitation forecasting: Recommendations from a USWRP workshop. *Bulletin of the American Meteorological Society*, *86*(11), 1619-1632. https://doi.org/10.1175/BAMS-86-11-1619

Ralph, F. M., Neiman, P. J., Wick, G. A., Gutman, S. I., Dettinger, M. D., Cayan, D. R., & White, A. B. (2006). Flooding on California's Russian River: Role of atmospheric rivers. *Geophysical Research Letters*, *33*(13). https://doi.org/10.1029/2006GL026689

Ralph, F. M., Intrieri, J., Andra Jr, D., Atlas, R., Boukabara, S., Bright, D., et al. (2013). The emergence of weather-related test beds linking research and forecasting operations. *Bulletin of the American Meteorological Society*, *94*(8), 1187-1211. https://doi.org/10.1175/BAMS-D-12-00080.1

Ralph, F. M., Dettinger, M., White, A., Reynolds, D., Cayan, D., Schneider, T., et al. (2014). A vision for future observations for western US extreme precipitation and flooding. *Journal of Contemporary Water Research & Education*, *153*(1), 16-32. https://doi.org/10.1111/j.1936-704X.2014.03176.x

Ralph, F. M., Cordeira, J. M., Neiman, P. J., & Hughes, M. (2016). Landfalling atmospheric rivers, the Sierra barrier jet, and extreme daily precipitation in Northern California's Upper Sacramento River watershed. *Journal of Hydrometeorology, 17*(7), 1905-1914. https://doi.org/10.1175/JHM-D-15-0167.1

Ralph, F. M., Rutz, J. J., Cordeira, J. M., Dettinger, M., Anderson, M., Reynolds, D., et al. (2019). A scale to characterize the strength and impacts of atmospheric rivers. *Bulletin of the American Meteorological Society*, *100*(2), 269-289. https://doi.org/10.1175/BAMS-D-18-0023.1

Ray, A. J., & White, A. B. (2019). The Hydrometeorology Testbed–West Legacy Observing Network: Supporting Research to Applications for Atmospheric Rivers and Beyond. *Atmosphere*, *10*(9), 533. https://doi.org/10.3390/atmos10090533

Rondanelli, R., Hatchett, B., Rutllant, J., Bozkurt, D., & Garreaud, R. (2019). Strongest MJO on record triggers extreme Atacama rainfall and warmth in Antarctica. *Geophysical Research Letters*, *46*(6), 3482-3491. https://doi.org/10.1029/2018GL081475

Rutz, J. J., Steenburgh, W. J., & Ralph, F. M. (2014). Climatological characteristics of atmospheric rivers and their inland penetration over the western United States. *Monthly Weather Review, 142*(2), 905-921. https://doi.org/10.1175/MWR-D-13-00168.1

Staley, D. M., Negri, J. A., Kean, J. W., Laber, J. L., Tillery, A. C., & Youberg, A. M. (2017). Prediction of spatially explicit rainfall intensity–duration thresholds for post-fire debris-flow generation in the western United States. *Geomorphology*, *278*, 149-162. https://doi.org/10.1016/j.geomorph.2016.10.019

Sterle, K., Hatchett, B. J., Singletary, L., & Pohll, G. (2019). Hydroclimate Variability in Snow-fed River Systems: Local Water Managers' Perspectives on Adapting to the New Normal. *Bulletin of the American Meteorological Society*, 100, 1031–1048, https://doi.org/10.1175/BAMS-D-18-0031.1

Swain, D. L. (2015). A tale of two California droughts: Lessons amidst record warmth and dryness in a region of complex physical and human geography. *Geophysical Research Letters*, *42*(22), 9999-10. https://doi.org/10.1002/2015GL066628

Thomas, M. A., Mirus, B. B., Collins, B. D., Lu, N., & Godt, J. W. (2018). Variability in soil-water retention properties and implications for physics-based simulation of landslide early warning criteria. *Landslides, 15*(7), 1265-1277. https://doi.org/10.1007/s10346-018-0950-z

Thomas, M. A., Collins, B. D., & Mirus, B. B. (2019). Assessing the feasibility of satellite-based thresholds for hydrologically driven landsliding. *Water Resources Research*, 55, 9006–9023. https://doi.org/10.1029/2019WR025577

Thorncroft, C. D., Hoskins, B. J., & McIntyre, M. E. (1993). Two paradigms of baroclinic-wave life-cycle behaviour. *Quarterly Journal of the Royal Meteorological Society*, *119*(509), 17-55. https://doi.org/10.1002/qj.49711950903

Uccellini, L. W., & Ten Hoeve, J. E. (2019). Evolving the National Weather Service to Build a Weather-Ready Nation: Connecting Observations, Forecasts, and Warnings to Decision Makers through Impact-Based Decision Support Services. *Bulletin of the American Meteorological Society*, 100, 1923–1942. https://doi.org/10.1175/BAMS-D-18-0159.1

Underwood, S. J., Kaplan, M. L., & King, K. C. (2009). The role of upstream midtropospheric circulations in the Sierra Nevada enabling leeside (spillover) precipitation. Part I: A synoptic-scale analysis of spillover precipitation and flooding in a leeside basin. *Journal of Hydrometeorology*, *10*(6), 1309-1326. https://doi.org/10.1175/2009JHM1106.1

Vilajosana, I., Khazaradze, G., Surinach, E., Lied, E., & Kristensen, K. (2007). Snow avalanche speed determination using seismic methods. *Cold regions science and technology*, *49*(1), 2-10. https://doi.org/10.1016/j.coldregions.2006.09.007

Wang, M., Wang, J., Bock, Y., Liang, H., Dong, D., & Fang, P. (2019). Dynamic Mapping of the Movement of Landfalling Atmospheric Rivers over Southern California with GPS Data. *Geophysical Research Letters*, *46*(6), 3551-3559. https://doi.org/10.1029/2018GL081318

White, A. B., Ralph, F. M., Neiman, P. J., Gottas, D. J., & Gutman, S. I. (2009, October). The NOAA coastal atmospheric river observatory. In *34th Conference on Radar Meteorology*. https://doi.org/10.3390/atmos10090533

White, A. B., Gottas, D. J., Henkel, A. F., Neiman, P. J., Ralph, F. M., & Gutman, S. I. (2010). Developing a performance measure for snow-level forecasts. *Journal of Hydrometeorology*, *11*(3), 739-753. https://doi.org/10.1175/2009JHM1181.1

White, A. B., Colman, B., Carter, G. M., Ralph, F. M., Webb, R. S., Brandon, D. G., et al. (2012). NOAA's rapid response to the Howard A. Hanson Dam flood risk management crisis. *Bulletin of the American Meteorological Society*, *93*(2), 189-207. https://doi.org/10.1175/Bams-D-11-00103.1

White, A. B., Anderson, M. L., Dettinger, M. D., Ralph, F. M., Hinojosa, A., Cayan, D. R., et al. (2013). A twenty-first-century California observing network for monitoring extreme weather

events. *Journal of Atmospheric and Oceanic Technology*, *30*(8), 1585-1603. https://doi.org/10.1175/JTECH-D-12-00217.1

White, A. B., Moore, B. J., Gottas, D. J., & Neiman, P. J. (2019). Winter storm conditions leading to excessive runoff above California's Oroville Dam during January and February 2017. *Bulletin of the American Meteorological Society*, *100*(1), 55-70. https://doi.org/10.1175/BAMS-D-18-0091.1

Wigmosta, M. S., Vail, L. W., & Lettenmaier, D. P. (1994). A distributed hydrology-vegetation model for complex terrain. *Water Resources Research*, *30*(6), 1665-1679. https://doi.org/10.1029/94WR00436

Wimmers, A. J., & Velden, C. S. (2010). Objectively determining the rotational center of tropical cyclones in passive microwave satellite imagery. *Journal of Applied Meteorology and Climatology*, *49*(9), 2013-2034. https://doi.org/10.1175/2010JAMC2490.1

Xiao, M., Koppa, A., Mekonnen, Z., Pagán, B. R., Zhan, S., Cao, Q., et al. (2017). How much groundwater did California's Central Valley lose during the 2012–2016 drought? *Geophysical Research Letters*, *44*(10), 4872-4879. https://doi.org/10.1002/2017GL073333

Zhang, D., Madsen, H., Ridler, M.E., Kidmose, J., Jensen, K.H. and Refsgaard, J.C., 2016. Multivariate hydrological data assimilation of soil moisture and groundwater head. *Hydrology and Earth System Sciences*, *20*(10), pp.4341-4357. https://doi.org/10.5194/hess-20-4341-2016